CONTEMPORARY AND INNOVATIVE RESEARCH IN NATURAL SCIENCE AND MATHEMATICS

All Sciences Academy

CONTEMPORARY AND INNOVATIVE RESEARCH IN NATURAL SCIENCE AND MATHEMATICS

Editor
Assoc. Prof. Dr. ALİ ÖZDEMİR

Contemporary and Innovative Research in Natural Science And Mathematics
Editor: Assoc. Prof. Dr. ALİ ÖZDEMİR

Design: All Sciences Academy Design
Published Date: March 2026
Publisher's Certification Number: 72273
ISBN: 978-625-8993-05-9

www.allsciencesacademy.com
allsciencesacademy@gmail.com

CONTENT

Investigating the Structural and Optical Properties of PVA/MgO with GNPs Nanocomposites

İbrahim KARTERİ[1]

Musa GÖĞEBAKAN[2]

1- Assoc. Prof. Dr.; bKahramanmaraş Istiklal University, Faculty of Elbistan Engineering, Department of Energy Systems Engineering, Kahramanmaraş, Türkiye, ibrahimkarteri@gmail.com ORCID No: 0000-0001-8913-6753

Prof. Dr.; aKahramanmaraş Sütçü İmam University, Faculty of Science, Department of Physics, Kahramanmaraş, Türkiye , gogebakan@ksu.edu.tr ORCID No: 0000-0001-5104-2874

ABSTRACT

Magnesium oxide (MgO) nanostructures combined with graphene nanoplatelets (GNPs) have garnered considerable attention in academic circles due to their wide-ranging applications in nanotechnology. This research successfully synthesized MgO nanoparticles at room temperature using magnesium chloride, urea, and sodium hydroxide. These nanoparticles were subsequently utilized to fabricate polyvinyl alcohol (PVA)/MgO-GNPs nanocomposites. The PVA/MgO-GNPs nanocomposite was developed through sol-gel methods, integrating MgO nanoparticles with cost-effective, industrial-grade GNPs. PVA polymer-based nanocomposites (PVA/MgO with GNPs) were prepared with varying concentrations of MgO (8 wt. %) and GNPs (1.5 and 3 wt. %). The structural properties of the synthesized PVA/MgO with GNPs nanocomposites were analyzed using X-ray diffraction (XRD), scanning electron microscopy (SEM), and Fourier transform infrared spectroscopy (FTIR). The SEM and FTIR findings confirmed the expected structural formation. Furthermore, the optical properties of the nanocomposites were assessed using UV-vis spectroscopy, and the energy band gap values were calculated. The PVA/MgO nanocomposites demonstrated potential for use in memristor devices.

Keywords – Graphene nanoplatelets, Magnesium oxide, Polymer, Optical properties, Nanocomposite

INTRODUCTION

Recently, researchers have been intensely focused on developing new and superior materials through the use of nanostructured materials. These materials demonstrate significantly enhanced mechanical, physical, and chemical properties. Nanostructured graphene and metal oxide materials, which offer a wide range of applications and whose potential uses are continually expanding, have captured considerable interest from the scientific community. As a result, this area has become a central focus of intensive research by materials scientists, physicists, and chemists. Metal oxide nanostructures, such as magnesium oxide (MgO), have drawn particular attention due to their crucial applications in electronic devices, electrocatalysis, refractory materials, and superconductors. Given their extensive and promising applications, metal oxide nanomaterials have been the subject of intensive study by researchers (Bdewi et al., 2016:326).

The synthesis of nano-structured materials, along with the examination of their properties and the identification of their potential applications, has been a subject of extensive research for many years. These materials are characterized by crystal sizes of less than 100 nm, and the uniform distribution of nanoparticles within the material significantly alters its properties. Nanocrystals that are evenly distributed within the material demonstrate substantial resistance to applied forces, thereby enhancing the mechanical properties of these materials. Additionally, they exhibit superior electronic properties. Notably, magnesium oxide and graphene nanostructures are increasingly significant in the production of polymer-based multifunctional nanocomposites due to their exceptional electronic properties. These nanostructured graphene and magnesium oxide materials confer valuable attributes to polymer materials through their intrinsic structures. Consequently, it is crucial to investigate magnesium oxide and graphene-doped polymer materials with high electronic properties and cost-effective production methods. Graphene, known for its remarkable tensile strength, electrical conductivity, mechanical flexibility, and exceptional chemical, structural, and thermal stability, is utilized in flexible electronic applications such as sensors (Sahatiya et al., 2016:25006), capacitors (Yang et al., 2018:419), batteries (Lu et al., 2018: 4614), memristors (Kim et al., 2018: 7335), and solar cells (Díez-Pascual et al., 2018: 2017). Magnesium oxide (MgO), an abundant and cost-effective material, is extensively employed in electronic applications due to its excellent electronic properties, including a wide band gap (~7.4 eV), high dielectric constant, and thermal conductivity. The development of nanocomposites with enhanced properties through the incorporation of graphene and magnesium oxide structures into polymers is essential for their application in electronic devices and systems (Yalagala et al., 2019: 104673).

In 2015, Sandeep et al. explored the straightforward growth of MgO micro-rods at low temperatures on multilayer graphene within a polyvinyl alcohol (PVA) matrix. They examined the growth mechanism of MgO micro-rods, the role of PVA in their development, and the observed morphological, structural, and phase characteristics, aiming for a more controlled synthesis (Marka et al., 2015:530). In 2016, Heidarizad et al. prepared graphene oxide/magnesium oxide (GO/MgO) nanocomposites

using graphene oxide structures, the oxidized form of graphene. These nanocomposites were characterized through scanning electron microscopy, transmission electron microscopy, X-ray diffraction, Fourier transform infrared spectroscopy, X-ray photoelectron spectroscopy, and thermogravimetric analysis. The results confirmed the successful decoration of MgO particles on GO, and they investigated the effects of various experimental variables on the GO/MgO structures (Heidarizad and Şengör, 2016:607). In 2017, Susan et al. synthesized MgO/PEG/GO nanocomposite materials using sol-gel and solyothermal methods. The microstructure of the nanocomposite, synthesized with three chemical compounds possessing adsorption properties, was examined using XRD, SEM, and FT-IR. They demonstrated the presence of MgO structures on nanosized GO structures based on SEM images, showing its effectiveness as a composite for ion removal (Samadi and Abbaszadeh, 2017:271). In 2018, Seham et al. synthesized graphene oxide (GO) from graphite using a chemical method. They characterized the prepared nanocomposites using XRD, Fourier transform infrared spectroscopy, and X-ray photoelectron spectroscopy, employing a simple precipitation method for creating hybrid nanocomposites MgO-rGO and Fe2O3-rGO. They also assessed the thermal properties of these hybrid nanocomposites (Abdel-Aal et al., 2018:1). In 2018, Kimiagar et al. synthesized magnesium oxide (MgO)-graphene oxide (GO) nanocomposites via a hydrothermal method at varying temperatures, investigating the impact of growth temperature on structural and linear and nonlinear optical parameters. Given the importance of discovering new materials for advancing optoelectronics, MgO-GO nanocomposites have shown potential applications in optical technology devices (Kimiagar and Abrinaei, 2018:243). In 2019, Pan et al. studied the role of graphene materials in enhancing the development of thermally conductive graphene/polymer nanocomposites. They specifically obtained composite structures using micro-sized MgO granules of controlled geometric size through a precipitation method, which allows for the simultaneous achievement of high surface activity (Pan et al., 2019:9).

This study focused on producing nanocomposite materials based on polyvinyl alcohol (PVA) doped with magnesium oxide (MgO) and graphene nanoplates (GNPs). To create innovative and high-value-added PVA-MgO-

GNPs nanomaterials, GNPs and chemically synthesized MgO structures were incorporated into a PVA polymer. The structural and optical properties of the resulting PVA/MgO structures with GNPs were thoroughly investigated.

MATERIALS AND METHOD

In this study, PVA/MgO nanocomposite materials with GNPs were obtained using the sol-gel method. PVA-based nanocomposite materials were produced by adding GNPs and MgO at different ratios to a PVA polymer material. GNPs (purity, 99.5 %; density, 0.05 g/cm3; thickness, 5–8 nm; and specific surface area, 150 m^2/g) were obtained from Graf Nano Technological Materials Industry and Trade Limited Company. PVA, sodium hydroxide (NaOH), urea, ethanol, and magnesium chloride ($MgCl_2$) were purchased from Sigma-Aldrich.

Synthesis of the MgO Materials

Firstly, a solution of 16 g Sodium Hydroxide (NaOH), 1 g Urea, 8 ml Ethanol and 50 ml distilled H2O was prepared in a beaker-A. Secondly, the solution of beaker-A was added to the solution of Magnesium Chloride ($MgCl_2$) prepared in distilled water in another beaker-B. The solutions in beakers A and B were transferred to each other and mixed at 60 °C with a magnetic stirrer. The resulting mixture was aged at 60 °C for 10 hours. Finally, white crystalline MgO materials were obtained by filtration with distilled water.

Preparation of the PVA-MgO Solution

First, a PVA solution was prepared by mixing 50 mL H_2O and 2 g PVA with a mechanical mixer at 70 ºC at 800 rpm. Then, an MgO solution prepared by adding 8 wt% MgO in 10 mL H_2O to the prepared PVA mixture was added. The obtained PVA-MgO mixture was mixed using a mechanical mixer, and a homogenous solution was obtained. For the optical and structural tests, the PVA-MgO solution was dried in an oven at 60ºC for 24 h, and a PVA-MgO composite material was produced.

Fabrication of the PVA/MgO with GNPs Nanocomposites

First, 1.5 wt% and 3 wt% of GNPs were added to the PVA-MgO solution obtained during the preparation of PVA/MgO with GNPs composites. The obtained solutions were then stirred with a magnetic stirrer for 24 h to obtain a new homogenous solution. Finally, PVA/MgO nanocomposite materials incorporating GNPs were produced by drying the solutions in Petri dishes at 60 °C for 24 h in an oven. The PVA/MgO nanocomposite materials incorporating GNPs were successfully synthesized with weight fractions as specified in Table 1. The resulting PVA/MgO nanocomposites with GNPs are shown in Fig. 1.

Table 1: % wt. compositions of the produced PVA/MgO nanocomposites with GNPs

Samples	***wt. % PVA***	***wt. % MgO***	***wt. % GNPs***
PVA-MgO	92.00	8.00	0.0
PVA-MgO with 1.5 wt % GNPs	90.62	7.88	1.5
PVA-MgO with 3 wt % GNPs	89.24	7.76	3.0

Characterization Techniques

UV-VIS spectroscopy was performed using a spectrophotometer (Shimadzu UV 1800). Fourier-transform infrared (FTIR) spectroscopy measurements were conducted using an FTIR spectrometer (Perkin Elmer Spectrum). The surface images of the produced PVA/MgO nanocomposite materials were obtained using a scanning electron microscope (SEM; Zeiss Evo). The crystal structures of PVA/MgO with GNPs nanocomposite materials were investigated using X-ray diffraction (XRD). Panalytical Philips X`Pert PRO brand XRD device was used in XRD Laboratory of Department of Physics, Kahramanmaras Sutcu Imam University. The operating parameters were determined using monochromatic Cu Kα radiation (λ=0.154056 nm) at 40 kV and 30 mA. Analysis measurements were taken from 20 °to 100 °at a speed of 0.02°/s.

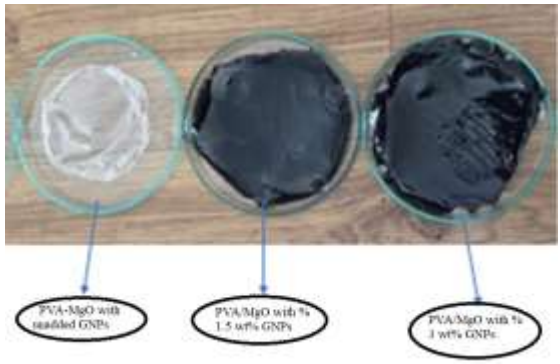

Figure 1: Fabricated PVA/MgO with GNPs nanocomposites.

RESULTS AND DISCUSSION

Ultraviolet–Vis Spectra

Figure 2 illustrates the absorption spectra of the prepared PVA/MgO nanocomposites with GNPs in various combinations. As depicted in Figure 2, both PVA/MgO with GNPs and nanocomposites without GNPs exhibit an absorption limit at low wavelengths ranging from 260 to 370 nm. This limit varies in PVA/MgO-GNPs nanocomposites produced without graphene and with different graphene additives. Notably, the spectra of the PVA-MgO structures display two absorption bands, observed at approximately 275 and 320 nm.

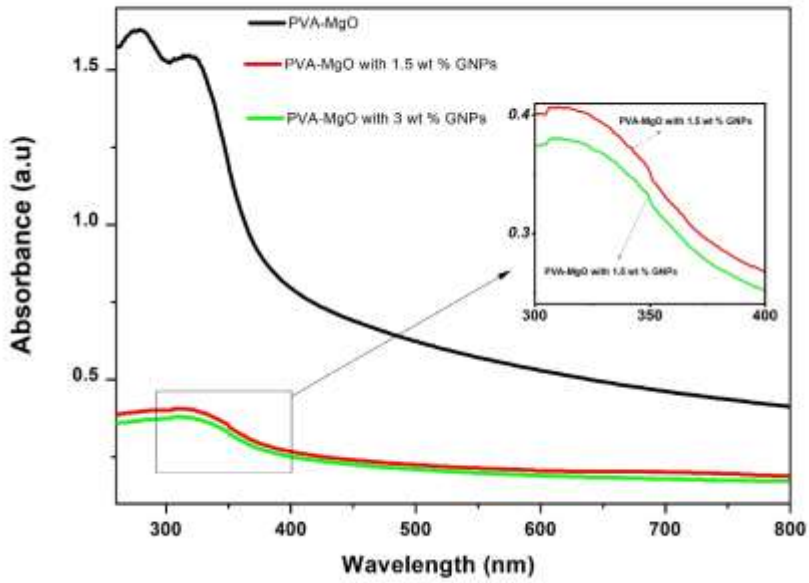

Figure 2: Absorption spectra of prepared PVA/MgO with GNPs nanocomposites in different combinations

However, when examining the PVA/MgO with GNPs nanocomposite structures, a hump band appears at around 325 nm. These bands in the Mg-PVA with GNPs nanocomposite structures may suggest the presence of carbonyl groups in PVA (Rudko et al., 2015:33). Equation (1) (Shinde et al., 2006:326:Water et al., 2002:998:Murali et al., 2010:350) was employed to determine the type of optical band gap using the basic absorption spectra of PVA/MgO-GNPs nanocomposite structures shown in Figure 2.

$$(\alpha h)=A(h-Eg)^{1/2} \quad (1)$$

In this context, h represents the photon energy, while A is a constant that does not depend on energy.

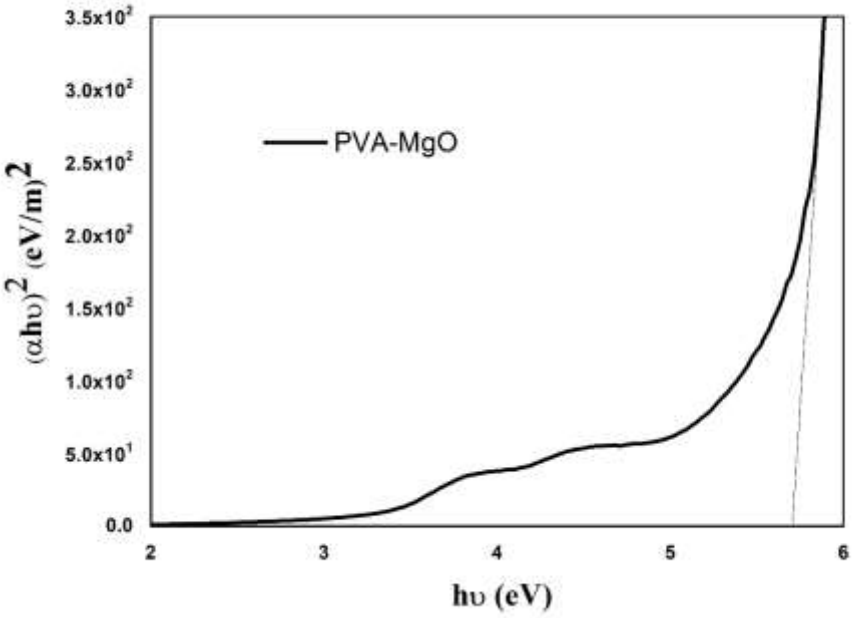

Figure 3: The plots of $(\alpha h\nu)^2$ against $(h\nu)$ for the PVA-MgO structures.

Figure 3 displays the plots of $(\alpha h)^2$ as a function of photon energy (h) for the PVA–MgO structures. In contrast, Figure 4 shows the plots of $(\alpha h)^2$ against photon energy (h) for the PVA–MgO structures that include GNPs. The direct band gap values were obtained by extrapolating the linear regions of these plots to the point of zero absorption, where $(\alpha h)^2 = 0$ (Uruş et al., 2017:133). The optical bandgap values for the PVA–MgO and PVA–MgO with GNPs nanocomposite structures were derived from Figures 3 and 4. The energy gap (Eg) value for the PVA–MgO structure, as indicated in Figure 3, was found to be 5.70 eV. Using the same approach, the Eg values for the PVA/MgO-1.5% wt GNPs and the PVA/MgO with 3% wt GNPs nanocomposites, as shown in Figure 4, were determined to be 5.60 eV and 5.49 eV, respectively. Analyzing these results reveals that the Eg value of the PVA–MgO nanocomposite material is the lowest. The addition of GNPs to the PVA–MgO structure resulted in a decrease in the Eg values.

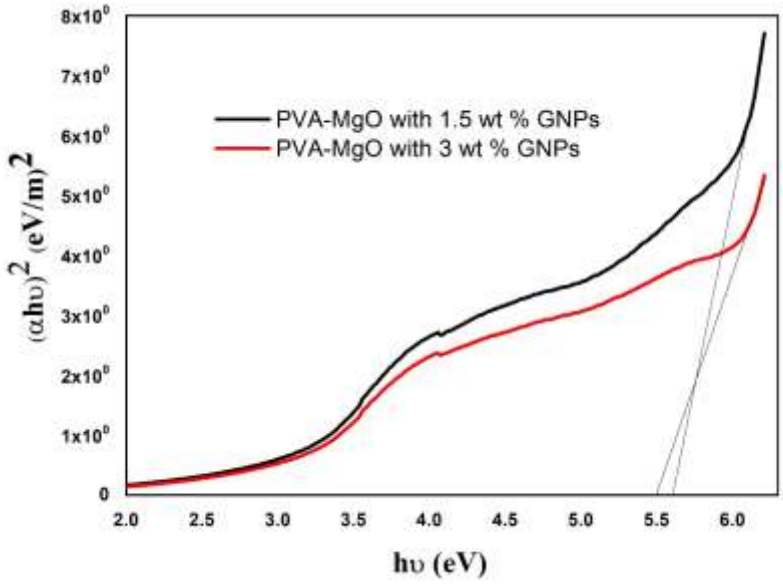

Figure 4: The plots of (αhν)2 against (hν) for the PVA-MgO with GNPs structures.

FTIR Spectra

The FTIR spectra of MgO nanoparticles were captured within the 400–4000 cm $^{-1}$ range, as illustrated in Fig. 5. A prominent peak in the MgO structures appears at a wavenumber of 3281 cm − 1, corresponding to the O–H stretching vibration group. The peak at 671 cm − 1 signifies Mg–O bond stretching, confirming the presence of Mg–O vibrations (Bdewi et al., 2016:326). The FTIR spectra of PVA and the synthesized PVA–MgO structures are presented in Fig. 6. The characteristic FTIR spectrum of PVA displays several bands, including O–H stretching, asymmetric and symmetric stretching of CH_2, and stretching of OH, C–O, and C–C. As shown in Fig. 6, the distinctive FTIR spectral peaks of the PVA structure are clearly observed at 2936 cm − 1 for the asymmetric stretching of CH2 and at 2906 cm − 1 for the symmetric stretching of CH2. Additionally, the FTIR bands of the PVA structure at 1083 and 1416 cm − 1 are attributed to the stretching of C–O and CH2 bending, respectively (Asran et al., 2010:868:Liu et al., 2010:203). As illustrated in Fig. 6, the peaks of the FTIR spectra of the prepared PVA–MgO nanocomposite materials closely align with those of the

PVA structure. However, Fig. 6 reveals a broadening of the PVA–MgO structure FTIR peaks when comparing PVA and PVA–MgO structures.

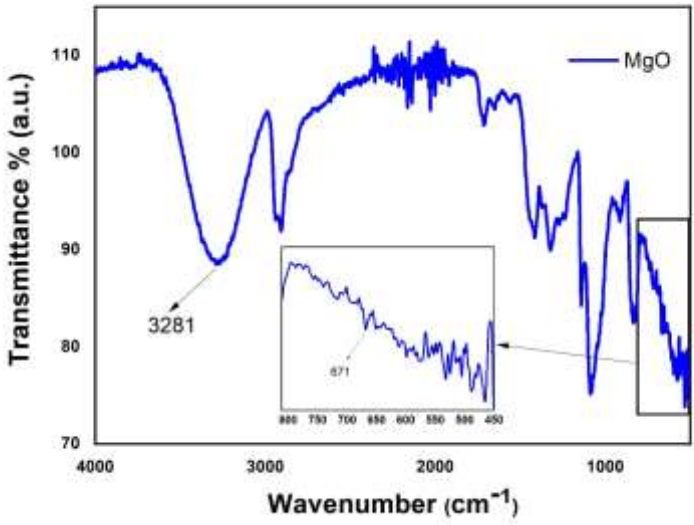

Figure 5: FTIR spectrum of the MgO structures.

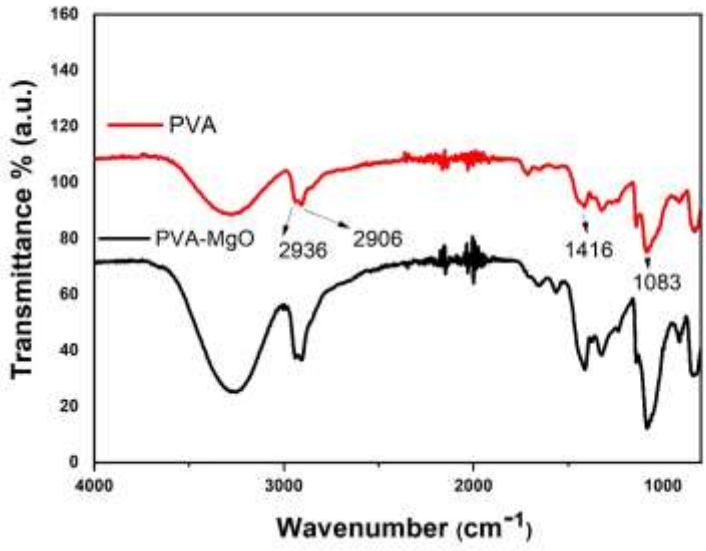

Figure 6: FTIR spectrum of the PVA and prepared PVA-MgO structures.

The FTIR spectra of PVA–MgO with 1.5 wt % GNPs and PVA–MgO with 3 wt % GNPs structures are shown in Fig. 7. As depicted in Fig. 7, the

PVA–MgO structures with 1.5 wt % and 3 wt % GNPs exhibit similar FTIR results. Consequently, when comparing PVA-MgO with 1.5 wt % GNPs and PVA-MgO with 3 wt % GNPs structures, produced with the addition of GNPs and MgO nanostructures, to PVA and PVA-MgO structures, slight shifts and changes in the peaks of the bond groups are observed.

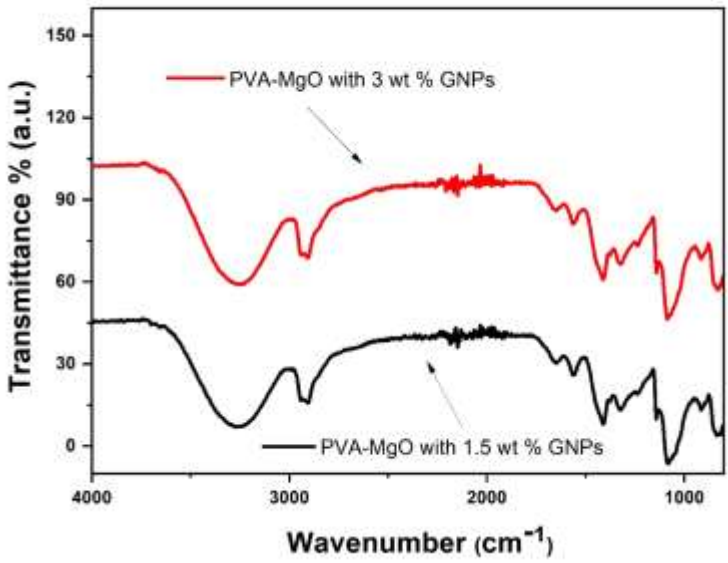

Figure 7: FTIR spectrum of prepared PVA-MgO with 1.5 wt % GNPs and PVA-MgO with 3 wt % GNPs structures.

Scanning Electron Microscopy (SEM)

In this study, the microstructures of the fabricated nanocomposites were examined using SEM. Fig. 8 presents SEM images of the prepared PVA-MgO structures at magnifications of (a) 3 KX and (b) 5 KX. As depicted in Fig. 8, the white spherical shapes within the PVA material signify the presence of an MgO structure. Notably, in the image of the PVA-MgO structure, the MgO material is uniformly distributed throughout the PVA. This homogeneous distribution is clearly observed due to MgO's unique structural characteristics and high specific surface area (Kinderlehrer et al., 2002:233: Warot et al., 2002:151).

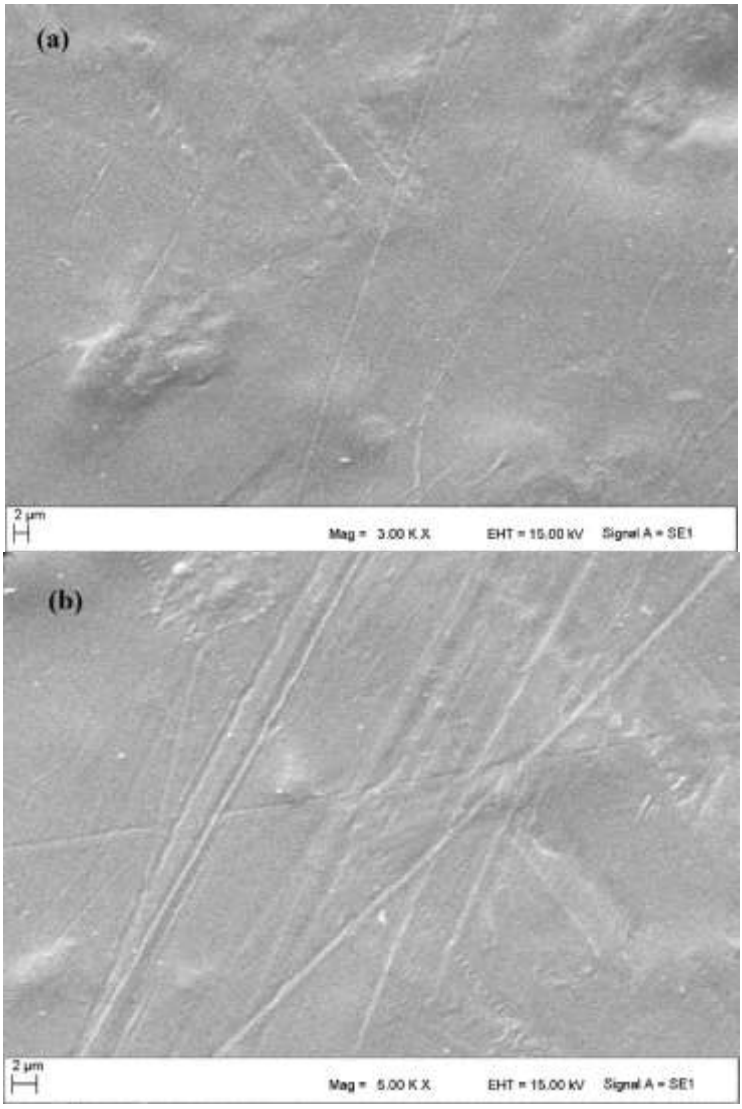

Figure 8: SEM image with a magnification of (a) 3 KX and (b) 5 KX of the prepared PVA-MgO structures.

SEM images of the prepared structures, (a) PVA-MgO with 1.5 wt % GNPs and (b) PVA-MgO with 3 wt % GNPs, are displayed in Fig. 9. As illustrated in Fig. 9 (a) and Fig. 9 (b), the morphological structures of the particles forming the microstructure of both PVA-MgO with 1.5 wt % GNPs and PVA-MgO with 3 wt % GNPs are identical. However, Fig. 9 (a) reveals that the SEM image of the PVA-MgO with 1.5 wt % GNPs nanocomposite material shows a significant impact on the microstructure due to the addition

of 1.5 wt % GNPs, resulting in changes to the particles forming the microstructure. Given the direct relationship between a material's microstructure and its properties, it is anticipated that changes in the microstructure will lead to alterations in the material's properties. Consequently, Fig. 9 demonstrates that the addition of GNPs to the prepared PVA-MgO materials alters the properties of the resulting PVA-MgO with GNPs (1.5 wt % and 3 wt %) nanocomposite material. Furthermore, as shown in Fig. 9 (b), increasing the GNPs ratio to 3 wt % in the nanocomposite material results in further observable changes.

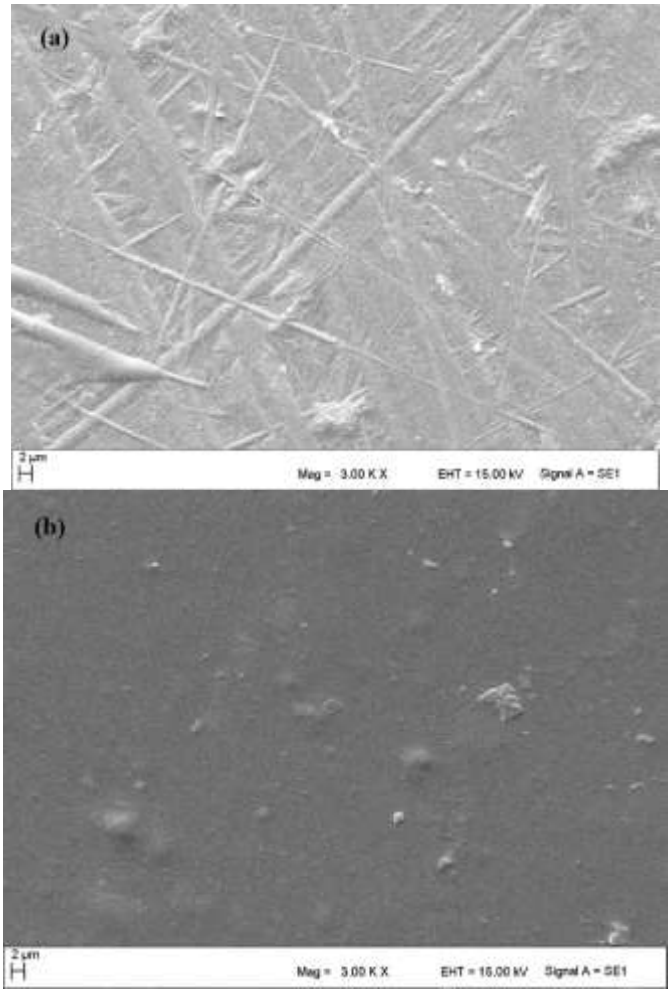

Figure 9: SEM image with a magnification of 3 KX of prepared (a) PVA-MgO with 1.5 wt % GNPs and (b) PVA-MgO with 3 wt % GNPs structures.

X-ray Diffraction (XRD)

Fig. 10 presents the XRD pattern of pure PVA powder, which is a semi-crystalline material. As depicted in Fig. 10, a prominent crystal reflection is observed at 219.27°, corresponding to the semi-crystalline phase of PVA. Additionally, Fig. 10 reveals that pure PVA material displays a characteristic peak at approximately 40°, indicative of its semi-crystalline nature (Abdullah et al., 2015:18: Gupta et al., 2009:186: Waly et al., 2021:2962: Aziz et al., 2017:486). This distinctive semi-crystalline structure of PVA arises from intramolecular and intermolecular hydrogen bonds, enabling the formation of such bonds between molecules of the same or different monomer units (Aziz et al., 2017:486: Abdullah et al., 2016:1103).

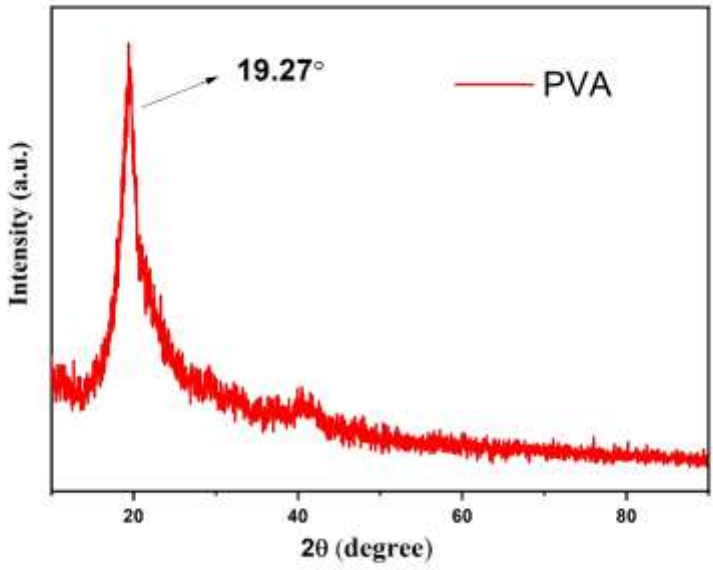

Figure 10: XRD pattern of pure PVA powder.

The XRD patterns of PVA-MgO with 1.5 wt % GNPs and PVA-MgO with 3 wt % GNPs are depicted in Fig. 11. As illustrated in Fig. 11, the XRD patterns for the PVA-MgO nanocomposite materials with 1.5 wt % and 3 wt % GNPs do not distinctly display the characteristic peaks of both MgO nanoparticles and GNPs nanostructured materials. Nonetheless, the XRD pattern of the resulting PVA-MGO-GNPs structures reveals a prominent peak at 219.27. Additionally, several other peaks appear at different angles

with very low intensities adjacent to this prominent peak. The absence of distinct peaks characteristic of MgO and GNPs is attributed to the very low concentrations of MgO and GNPs structures relative to the semi-crystalline PVA polymer. Consequently, it is not feasible to clearly demonstrate the contribution of MgO and GNPs in the XRD patterns of PVA-MGO-GNPs structures. However, other structural properties of the produced PVA-MGO-GNPs structures were determined using FTIR.

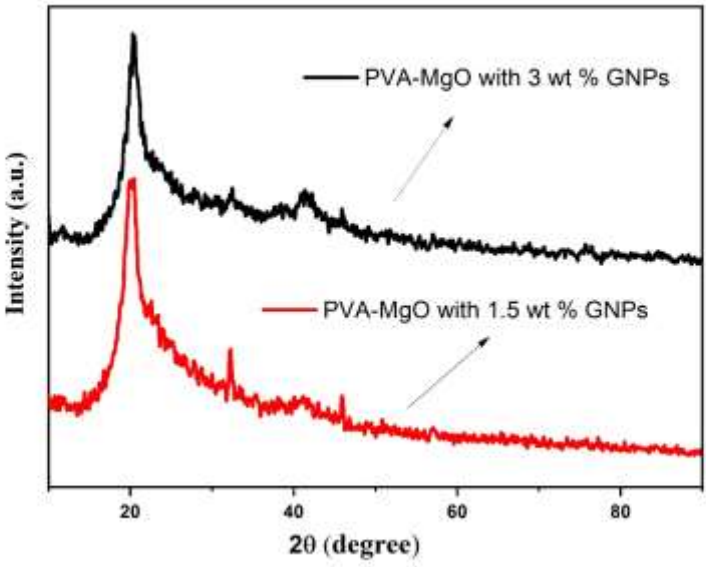

Figure 11: XRD pattern of PVA-MgO with 1.5 wt % GNPs and PVA-MgO with 3 wt % GNPs structures.

CONCLUSIONS

In this study, MgO nanoparticles were effectively synthesized using the sol-gel method. Subsequently, nanocomposite structures of PVA-MgO containing 8 wt % were produced with the synthesized MgO. These PVA-MgO structures were then doped with 1.5 and 3 wt % GNPs, leading to the creation of PVA-MgO with 1.5 wt % GNPs and PVA-MgO with 3 wt % GNPs nanocomposite materials. The structural properties of the resulting PVA-MgO-GNPs structures were analyzed using PXRD and FTIR, while SEM was employed to examine their morphological properties. Additionally, the optical properties of the prepared PVA-MgO-GNPs

nanocomposite structures were investigated. The Eg values for the nanocomposites PVA-MgO, PVA/MgO with 1.5 wt % GNPs, and PVA/MgO containing 3 wt % GNPs were determined to be 5.70, 5.60, and 5.49 eV, respectively. The results indicate that the Eg values decrease when MgO and GNPs are doped into the PVA polymer material.

Acknowledgements

This study received partial funding from Graf Nano Technological Materials Industry and Trade Ltd. Co. The authors are also grateful to the Kahramanmaras Sutcu Imam University Scientific Research Projects Coordination Unit (Project No: 2020/06-6 M) for their financial assistance.

REFERENCE

Sahin, S., Ocak, M.A., ve Uluyol, C.(2009). A systematic evaluation of preservice teachers' opinions on learning objects. International Journal of Human Sciences, 6(2), 723-736.

Bdewi, S. F., Abdullah, O. G., Aziz, B. K., Mutar, A. A. (2016). Synthesis, structural and optical characterization of MgO nanocrystalline embedded in PVA matrix. Journal of Inorganic and Organometallic Polymers and Materials, 26, 326-334.

Sahatiya, P., Puttapati, S. K., Srikanth, V. V., Badhulika, S. (2016). Graphene-based wearable temperature sensor and infrared photodetector on a flexible polyimide substrate. Flexible and Printed Electronics, 1(2), 025006.

Yang, J., Weng, W., Zhang, Y., Du, X., Liang, Y., Yang, L., Zhu, M. (2018). Highly flexible and shape-persistent graphene microtube and its application in supercapacitor. Carbon, 126, 419-425.

Lu, C., Li, Z., Yu, L., Zhang, L., Xia, Z., Jiang, T., Sun, J. (2018). Nanostructured Bi 2 S 3 encapsulated within three-dimensional N-doped graphene as active and flexible anodes for sodium-ion batteries. Nano Research, 11, 4614-4626.

Kim, S., Jung, H. J., Kim, J. C., Lee, K. S., Park, S. S., Dravid, V. P., Jeong, H. Y. (2018). In situ observation of resistive switching in an asymmetric graphene oxide bilayer structure. ACS nano, 12(7), 7335-7342.

Díez-Pascual, A. M., Luceño Sánchez, J. A., Peña Capilla, R., García Díaz, P. (2018). Recent developments in graphene/polymer nanocomposites for application in polymer solar cells. Polymers, 10(2), 217.

Yalagala, B., Khandelwal, S., Deepika, J., Badhulika, S. (2019). Wirelessly destructible MgO-PVP-Graphene composite based flexible transient memristor for security applications. Materials Science in Semiconductor Processing, 104, 104673.

Marka, S. K., Mohiddon, M. A., Prasad, M. D., Srikanth, V. V. (2015). Growth of MgO on multi-layered graphene and Mg in PVA matrix. Superlattices and Microstructures, 83, 530-537.

Heidarizad, M., Şengör, S. S. (2016). Synthesis of graphene oxide/magnesium oxide nanocomposites with high-rate adsorption of methylene blue. Journal of Molecular Liquids, 224, 607-617.

Samadi, S.,Abbaszadeh, M. (2017). Synthesis and characterization of MgO/PEG/GO nanocomposite and its application for removal of copper (II) from aquatic media. ACS Nano, 86, 271-280.

Abdel-Aal, S. K., Ionov, A., Mozhchil, R. N., Naqvi, A. H. (2018). Simple synthesis of graphene nanocomposites MgO–rGO and Fe 2 O 3–rGO for multifunctional applications. Applied Physics A, 124, 1-10.

Kimiagar, S., Abrinaei, F. (2018). Effect of temperature on the structural, linear, and nonlinear optical properties of MgO-doped graphene oxide nanocomposites. Nanophotonics, 7(1), 243-251.

Pan, W., He, M., Zhang, L., Hou, Y., Chen, C. (2019). Interfacial engineering of graphene nanosheets at mgo particles for thermal conductivity enhancement of polymer composites. Nanomaterials, 9(5).

Rudko, G. Y., Kovalchuk, A. O., Fediv, V. I., Chen, W. M., & Buyanova, I. A. (2015). Interfacial bonding in a CdS/PVA nanocomposite: A Raman scattering study. Journal of colloid and interface science, 452, 33-37.

Shinde, V. R., Gujar, T. P., Lokhande, C. D., Mane, R. S.,Han, S. H. (2006). Mn doped and undoped ZnO films: A comparative structural, optical and electrical properties study. Materials Chemistry and Physics, 96(2-3), 326-330.

Water, W., Chu, S. Y., Juang, Y. D., Wu, S. J. (2002). Li2CO3-doped ZnO films prepared by RF magnetron sputtering technique for acoustic device application. Materials Letters, 57(4), 998-1003.

Murali, K. R., Kalaivanan, A., Perumal, S., Pillai, N. N. (2010). Sol–gel dip coated CdO: Al films. Journal of Alloys and Compounds, 503(2), 350-353.

Uruş, S., Adıgüzel, H., Keleş, M., & Karteri, I. (2017). Multi-walled carbon nanotube supported aminomethylphosphine-Ru (II) complexes: Optical behavior and catalytic properties in transfer hydrogenation of acetophenone

derivatives. Fullerenes, Nanotubes and Carbon Nanostructures, 25(2), 133-141.

Asran, A. S., Henning, S., & Michler, G. H. (2010). Polyvinyl alcohol–collagen–hydroxyapatite biocomposite nanofibrous scaffold: Mimicking the key features of natural bone at the nanoscale level. Polymer, 51(4), 868-876.

Liu, Y., Geever, L. M., Kennedy, J. E., Higginbotham, C. L., Cahill, P. A., & McGuinness, G. B. (2010). Thermal behavior and mechanical properties of physically crosslinked PVA/Gelatin hydrogels. Journal of the mechanical behavior of biomedical materials, 3(2), 203-209.

Kinderlehrer, D., Ta'asan, S., Livshits, I., & Mason, D. E. (2002). The surface energy of mgo: Multiscale reconstruction from thermal groove geometry. Interface Science, 10, 233-242.

Warot, B., Snoeck, E., Ousset, J. C., Casanove, M. J., Dubourg, S., & Bobo, J. F. (2002). Surface morphology of NiO layers on MgO (0 0 1), MgO (1 1 0) and MgO (1 1 1). Applied surface science, 188(1-2), 151-155.

Abdullah, O. G., Salman, Y. A., & Saleem, S. A. (2015). In-situ synthesis of PVA/HgS nanocomposite films and tuning optical properties. Physics and Materials Chemistry, 3(2), 18-24.

Gupta, S., Pramanik, A. K., Kailath, A., Mishra, T., Guha, A., Nayar, S., & Sinha, A. (2009). Composition dependent structural modulations in transparent poly (vinyl alcohol) hydrogels. Colloids and Surfaces B: Biointerfaces, 74(1), 186-190.

Waly, A. L., Abdelghany, A. M., & Tarabiah, A. E. (2021). Study the structure of selenium modified polyethylene oxide/polyvinyl alcohol (PEO/PVA) polymer blend. Journal of Materials Research and Technology, 14, 2962-2969.

Aziz, S. B., Abdulwahid, R. T., Rasheed, M. A., Abdullah, O. G., & Ahmed, H. M. (2017). Polymer blending as a novel approach for tuning the SPR peaks of silver nanoparticles. Polymers, 9(10), 486.

Abdullah, O. G., Aziz, S. B., & Rasheed, M. A. (2016). Structural and optical characterization of PVA: KMnO4 based solid polymer electrolyte. Results in physics, 6, 1103-1108.

Graphene in de-Sitter and Anti-de-Sitter Spaces

Lakhdar Sek[*]

Sayah Rezgui [2]

Mokhtar Falek[3]

Mustafa Moumni [3]

[1,2,3]Laboratory of PhotonicPhysics and Nano-Materials (LPPNM), University of Biskra- Biskra, Algeria.
[*]lakhdar.sek@univ-biskra.dz

ABSTRACT

This work, we study (2+1) dimensional massless Dirac equation within a uniform magnetic field in the commutation relations of the Anti /de-Sitter space. Where the energy eigenvalues and the corresponding wave functions are obtained using the Nikiforov-Uvarov method after submission of this latter in the extended uncertainty principle of Heisenberg in order to show the curvature of the space. We find the findings have been affected by the studied deformation of the dS which has a hard confinement for large values of n^2 (the principal quantum number).

Keywords – Graphene, Anti /deSitter Space, Thermodynamic Properties.

I. INTRODUCTION

Carbon in its allotropic forms such as graphite and diamond occupies a prominent place in various branches of science. In particular, one can imagine that graphite consists of the accumulation of thick layers of carbon in an atom, the so-called graphene. The theoretical scientific community, since experimental observations revealed the existence of electrical charge carriers that behave like massless Dirac quasi-particles [1-4]. The reason for this lies in the unusual molecular structure of graphene. Carbon atoms are arranged in a hexagonal lattice, similar to a honeycomb structure [5]. It has been observed that low-energy electronic excitations at the corners of the Brillouin zone of graphene can be described by (2 + 1) Dirac fermions with a linear scattering ratio (massless) [3, 4]. This effect offers the opportunity to test various aspects of relativistic phenomena, which generally require high energy, in experiments in condensed matter physics, such as: the chiral tunnel and the Klein paradox [6, 7]

On the other hand, among the various attempts to integrate gravity into the quantum world, there is one area that has generated great interest; it is the quantum theory of fields in curved space through generalizations of Heisenberg algebra, such as the extended uncertainty principle (EUP). The purpose of this extended principle is to account for the quantum fluctuations of the gravitational field in order to include gravity in the quantum mechanics domain. One of the consequences of this standardization is the existence of a minimal length scale of the Planck order [8]. We can combine this minimum length with a modification of Heisenberg's standard algebra by adding small corrections to the canonical commutation relations and thus changing their standard algebra; we quote here the work of Mignemi [8], who showed that Heisenberg relations in the (anti-) deSitter space are modified by adding corrections that are proportional to the cosmological constant. These modifications were also motivated by Doubly Special Relativity (DSR) [9, 10], string theory [11], non-commutative geometry [12] and black hole physics [13, 14]. Effects of Newtonian gravity in quantum systems [15] and the modification of inertia, which

is predicted by some alternative theories of gravity on cosmic scales, can be derived naturally within the framework of the EUP [16].

In recent years, a large part of the research work has been devoted to the study of relativistic quantum mechanics with the EUP [17-19]. Some problems have also been solved in non-relativistic quantum mechanics; this happened despite the fact that we cannot derive any non-relativistic Schrödinger-like covariant equations from the Klein-Fock-Gordon covariant equation in the traditional field theoretical method of the deSitter (dS) models and anti-deSitter (AdS) [20-22].

In this work, we are interested in phenomenological models of quantum gravity. We study analytically in 2D spaces, the massless Dirac equation in the position space representation for deformed quantum mechanics with EUP in an interaction with an external uniform magnetic field for this system. The paper is organized as follows: In Sec.2, we provide an analysis of the AdS /dS model while in Sec.3; we introduce the Nikiforov–Uvarov (NU) method used to solve the equation of our system. We expose in Sec.4 the explicit calculations of both eigenfunctions and eigenvalues of the deformed 2D graphene in a uniform magnetic field with AdS/dS algebra. To sum up with a conclusion in Sec.6.

II. Review of Quantum Mechanics Relations

We may introduce some relations in the deformed quantum mechanics such the deformed Heisenberg algebra leading to the EUP of Ads space given [9-10]

$$\left[\boldsymbol{X_i}, \boldsymbol{X_j}\right] = \mathbf{0}\,; \left[\boldsymbol{P_i}, \boldsymbol{P_j}\right] = -\boldsymbol{i\hbar\lambda\epsilon_{ijk}}\, \boldsymbol{L_k}\,; \left[\boldsymbol{X_i}, \boldsymbol{P_j}\right] = \boldsymbol{i\hbar}\left(\boldsymbol{\delta_{ij}} - \boldsymbol{\lambda X_i X_j}\right) \quad (1)$$

λ is a small positive deformation parameter.

L_k is the angular momentum variable, expressed as follows :

$$\boldsymbol{L_k} = \boldsymbol{\epsilon_{ijk} X_i P_i} \quad (2)$$

The usual algebra is written:

$$\left[L_i, P_j\right] = i\hbar\varepsilon_{ijk}P_k\,;$$

$$\left[L_i, X_j\right] = i\hbar\varepsilon_{ijk}X_k\,; \left[L_i, L_j\right] = i\hbar\varepsilon_{ijk}L_k \quad (3)$$

The Ads model (1) deformed algebra is defined by the existence of a minimum uncertainty in momentum that is nonzero and gives rise to modified Heisenberg uncertainty relationships:

$$\boldsymbol{\Delta X_i \Delta P_i} \geq \frac{\hbar}{\mathbf{2}}\left(\mathbf{1} \pm \boldsymbol{\lambda}(\boldsymbol{\Delta X_i})^2\right) \quad (4)$$

The non-commutative operators X_i andP_i as functions of the usual x_i and p_i operators will be used to satisfy the ds algebra (1),

$$\boldsymbol{X_i} = \frac{\boldsymbol{x_i}}{\sqrt{\mathbf{1} \pm \boldsymbol{\lambda r^2}}}; \boldsymbol{P_i} = -\boldsymbol{i\hbar}\sqrt{\mathbf{1} \pm \boldsymbol{\lambda r^2}}\boldsymbol{\partial x_i} \quad (5)$$

III. Massless Dirac Equation in AdS and dS

The electron in quantum theory of graphene is a massless fermion that moves at a velocity $V_F = (1.12 \pm 0.02) \times 10^6\ ms^{-1}$, called the Fermi velocity verify the relativistic massless Dirac equation. The discovery of graphs gives us the opportunity to test various effects of QED, such as the "small paradox", since this effect cannot be observed in particle physics [28]. In this section, we are interested in solving the Dirac equation without dimensional mass (1 + 2) in the presence of a constant external magnetic field $\overrightarrow{A} = \frac{B}{2}(-y, x, 0)$. The Hamiltonian of the massless (2+1)-dimensional Dirac equation is [29];

$$(\hat{\boldsymbol{\alpha}}.\mathbf{p})\Psi(r) = \frac{E}{V_F}\Psi(r)$$

Where $\hat{\alpha}$ is the usual Dirac matrices and we may assume that the four-component spinor Ψ is of the form $\Psi(r) = (\Psi_a(r), \Psi_b(r))$.

We use the AdS algebra definition (eqs.6 and 7) and involving the spinor above, to rewrite this equation in the deformed momentum space:

$$\hat{\boldsymbol{\sigma}}.(\mathbf{p} - \mathbf{eA})\boldsymbol{\Psi}_{\mathbf{b}}(\mathbf{r}) = \frac{E}{V_F}\boldsymbol{\Psi}_{\mathbf{a}}(\mathbf{r}) \qquad \textbf{(19-a)}$$

$$\hat{\boldsymbol{\sigma}}.(\mathbf{p} - \mathbf{eA})\boldsymbol{\Psi}_{\mathbf{a}}(\mathbf{r}) = \frac{E}{V_F}\boldsymbol{\Psi}_{\mathbf{b}}(\mathbf{r}) \qquad (19\text{-b})$$

With $\hat{\sigma}$ designates the Pauli matrices. Then, we eliminate $\Psi_b(r)$ in favor of $\Psi_a(r)$, to obtain the following equation:

$$[\hat{\boldsymbol{\sigma}}.(\mathbf{p} - \mathbf{eA})]^2\boldsymbol{\Psi}_{\mathbf{a}}(\mathbf{r}) = \frac{E^2}{V_F{}^2}\boldsymbol{\Psi}_{\mathbf{a}}(\mathbf{r})$$

According to the following relations:

$$(\hat{\boldsymbol{\sigma}}.\mathbf{A})(\hat{\boldsymbol{\sigma}}.\mathbf{B}) = \mathbf{A}.\mathbf{B} + \mathbf{i}\hat{\boldsymbol{\sigma}}.(\mathbf{A} \times \mathbf{B}) \qquad (21)$$

The eq (20) becomes:

$$(\mathbf{p}^-.\mathbf{p}^- + \mathbf{i}\hat{\boldsymbol{\sigma}}.(\mathbf{p}^- \times \mathbf{p}^-))\boldsymbol{\Psi}_{\mathbf{a}}(\mathbf{r}) = \frac{\mathbf{E}^2}{\mathbf{V_F}^2}\boldsymbol{\Psi}_{\mathbf{a}}(\mathbf{r}) \qquad (22)$$

Where $p^- = \left(\sqrt{1 \pm \lambda r^2}\,p - \left(\frac{eB}{2}\right)\left(\frac{-y}{\sqrt{1\pm\lambda r^2}}\vec{\imath} + \frac{x}{\sqrt{1\pm\lambda r^2}}\vec{\jmath}\right)\right)$.

After a straightforward calculation of eq (22), we obtain:

$$\left[(1 \pm \lambda r^2)p^2 + \alpha\frac{r^2}{1\pm\lambda r^2} + i\hbar\lambda r.p - \gamma L_z - eB\hbar\sigma_z - \frac{E^2}{V_F{}^2}\right]\Psi_a(r) = 0 \quad (23)$$

Here the parameters;

$$\alpha = \frac{e^2B^2}{4} - \frac{eB}{2}\lambda\hbar\sigma_z \quad (24)$$

$$\gamma = eB + \lambda\hbar\sigma_z \quad (25)$$

To solve the eq.(23), we introduce the polar coordinates in position space (r, ϕ), and we use the following ansatz $\Psi_a(r) = \exp(im_l\varphi)R_{n,l}(r)\chi_\tau$, where n is the radial quantum number, m_l and $\tau = \pm 1$ are, respectively, the eigenvalues of angular momentum and spin operators, and $\chi^T_{+1} = (1,0)$, $\chi^T_{-1} = (0,1)$ are the spin functions; to obtain

$$\left[(1 \pm \lambda r^2)\left(\frac{d}{dr}\right)^2 - \frac{m_l^2(1\pm\lambda r^2)}{r^2} - \frac{\eta r^2}{\hbar^2(1\pm\lambda r^2)} + \varepsilon\right]R_{n,l}(r) = 0 \quad (26)$$

With

$$\eta = \frac{\hbar^2}{4l_B^4} - \frac{\lambda\hbar^2}{2l_B^2}\tau \quad (27)$$

$$\varepsilon = \frac{E^2}{\hbar^2 V_F{}^2} + \frac{\tau}{l_B^2} + m_l\left(\frac{1}{l_B^2} + \lambda\tau\right) \quad (28)$$

Where $l_B = \sqrt{\frac{\hbar}{eB}}$ is the fundamental length scale in the presence of a magnetic field.

We consider the transformations and the proceeding steps to follow by using the Nikiforov-Uvarov (NU) in order to obtain the energy spectrum and the corresponding wave function as in Ref [30].

Until we get the energy spectrum in the form:

$$E^{\lambda}_{n,m_l,\tau} = \pm\frac{\hbar V_F}{l_B}[(2n + m_l + 1)\sqrt{(2\lambda l_B^2\tau \pm \lambda^{2l_B4})} + \lambda l_B{}^2(4n(n + m_l + 1) + (2 - \tau)m_l + 1) - (m_l + \tau)]^{\frac{1}{2}} \quad (29)$$

We notice that the energy spectrum of our system has n^2 dependence of the energy levels, which corresponds to a confinement at the high-energy area; our result is

equivalent to the energy of a spinless relativistic quantum particle in a square well potential.

Now, let us conclude the corresponding wave function after employing and following the steps as NU method to get that form;

$$\begin{aligned}&\boldsymbol{\Psi_n(r,\phi)}\\&\boldsymbol{= C_n 2^{\frac{m_l}{2}} \exp\left(i m_l \phi\right)(1}\\&\boldsymbol{-\lambda r^2)^{\mu/2}(\lambda r^2)^{\frac{m_l}{2}} P_n^{(m_l,\mu-1/2)}(1}\\&\boldsymbol{-2\lambda r^2)}\end{aligned} \tag{30}$$

Where C_n is the normalization constant.

We can test this finding in many ways such as; if we put$\lambda = 0$, we obtain the ordinary expression of the spectrum in the usual space [31]

$$\boldsymbol{E^0_{n,0,1} = \pm \frac{\hbar V_F}{l_B}\sqrt{2n}} \tag{31}$$

IV. CONCLUSION

In this paper, we investigated the exact solutions of the 2D massless Dirac equation with a uniform external magnetic field in the context of deformed quantum mechanics with de-Sitter and anti-deSitter commutation relationships. These AdS deformations lead to a minimal non-zero uncertainty in the measurement of the momentum. The NikiforovUvarov method was used and thus we get the analytical expressions of the bound state energies and the wave functions of the system, in this case, we express the functions analytically in terms of the system in relation on Jacobi's polynomials and the corresponding eigenenergy's with additional corrections depending on the deformation parameter λ. Our results show that the deformed spectrum remains discrete even with large values of the principal quantum number and thus the EUP deformation eliminates the degeneracy of the spectrum (no deformations) found in the normal case.

REFERENCES

[1] K.S. Novoselov, et al. Science 306 (2004) 666.
[2] K.S. Novoselov, et al. Proc. Natl. Acad. Sci. 102 (2005) 10451.
[3] A.H. Castro Neto, F. Guinea, N.M.R. Peres, K.S. Novoselov, A.K. Geim, Rev. Modern Phys. 81 (2009) 109.
[4] N. Peres, Rev. Modern Phys. 82 (2010) 2673.
[5] Charles L. Fefferman, Michael I. Weinstein, J. Amer. Math. Soc. 25 (2012) 1169.
[6] M.I. Katsnelson, K.S. Novoselov, A.K. Geim, Nat. Phys. 2 (2006) 620.

[7] M.I. Katsnelson, Mater. Today 10 (2007) 20.
[8] S. Mignemi. Mod.Phys. Lett. A 25, 1697 (2010) 17
[9] G. Amelino-Camelia. Phys. Lett. B 510,255 (2001)
[10] G. Amelino-Camelia. Int. J. Mod. Phys. D 11, 35 (2002)
[11] S. Capozziello, G. Lambiase, G. Scarpetta. Int. J. Theor. Phys. 39, 15 (2000)
[12] M.R. Douglas and N.A. Nekrasov. Rev. Mod. Phys. 73, 977 (2001)
[13] F. Scardigli. Phys. Lett. B 452, 39 (1999)
[14] F. Scardigli and R. Casadio. Class. Quant. Grav. 20, 3915 (2003)
[15] V.E. Kuzmichev and V.V. Kuzmichev. Eur. Phys. J. C 80, 248 (2020)
[16] J. Gin´e and G. G. Luciano. Eur. Phys. J. C 80, 1039 (2020)
[17] B. Hamil and M. Merad. Eur. Phys. J. Plus 133, 174 (2018)
[18] W.S. Chung, H. Hassanabadi and N. Farahani. Mod. Phys. Lett. A 34, 1950204 (2019)
[19] M. Hadj Moussa and M. Merad. Few-Body Syst. 59, 44 (2018)
[20] B. Hamil, M. Merad and T. Birkandan. Eur. Phys. J. Plus 134, 278 (2019)
[21] S. Ghosh and S. Mignemi. Int. J. Theor. Phys. 50,1803 (2011)
[22] M. Falek, N. Belghar and M. Moumni. Eur. Phys. J. Plus. 135, 335 (2020)
[23] S. Mignemi. Class.Quant. Grav. 29, 215019 (2012)
[24] M.M. Stetsko. J. Math. Phys. 56, 012101(2015)
[25] B. Bolen, M. Cavagli`a. Gen. Relativ. Gravit. 37, 1255–1262 (2005)
[26] H. Egrifes, D. Demirhan, F. Buyukkili¸c. Phys. Scripta 59, 195–198 (1999)
[27] A.F. Nikiforov, V.B. Uvarov, Special Functions of Mathematical Physics (Birkhauser, Basel, 1988).
[28] A.D. Guclu, P. Potasz, M. Korkusinski, P. Hawrylak, Graphene Quantum Dots (Springer, Berlin, 2014)
[29] Hamil, B., & Merad, M. Few-Body Systems, 60(2), 36. (2019)
[30] Sek, Lakhdar, Mokhtar Falek, and Mustafa Moumni. Int. J. Mod.Phys.A.2150113 (2021)
[31] V. Santos, R.V. Maluf, C.A.S. Almeida, Ann. Phys. 349, 402 (2014)

Exact Solution of 2D Graphene in Non-Commutative Geometry and its Thermal Properties

Lakhdar Sek[*]

Mokhtar Falek [2]

Mustafa Moumni [3]

[1,2, 3]Laboratory of Photonic Physics and Nano-Materials (LPPNNM), Department of Matter Sciences, University of Biskra, Biskra. Algeria. [*]lakhdar.sek@univ-biskra.dz

ABSTRACT

The 2+1 dimensional Dirac massless equation in non-commutative geometry is investigated in this paper under the influence of a uniform magnetic field. We solve the system analytically using a direct method to obtain the energy eigenvalues and corresponding wave functions by taking the confluent hypergeometric functions to solve the system. Finally, we analyze the thermodynamic properties of the graphene in NC space with the help of the partition function Z and we showed that the results and the thermal features have been affected by the studied geometry.

Keywords – Graphene, Non-Commutative Geometry, Thermodynamic Properties.

I. INTRODUCTION

Non-commutative space is gaining popularity in the field and string theories [1]. Snyder was the first to explain the lack of change in space-time coordinates [2], and this principle offers stimulating scenarios in a number of unifying interaction theories known as M-Theory [3-4] as well as modern cosmology [5-7]. The formula's application is not limited to the following areas: non-commutative theory can explain the fusion of ultraviolet and infrared radiation in very small areas [8, 9], Lorentz symmetry breaking [10-11], and field quantum physics [10-11]. There have also been extensive studies on the integration of non-commutative relationships in ordinary quantum mechanics and classical geometry [12-14]. Furthermore, in recent years, changing normal relationships and nondeterministic relationships inspired by string theory, quantum gravity, and special relativity have been the focus of very interesting research [15-18].

Graphite is the accumulation of thick layers of carbon in an atom known as graphene. The physics of graphene has piqued the interest of theoretical scientists, with experimental observations revealing the existence of electrical charge carriers that behave like massless Dirac quasiparticles [19- 22]. The reason for this is due to graphene's unique molecular structure. Carbon atoms are arranged in a hexagonal lattice, similar to that of a honeycomb [23]. Low-energy electronic excitations have been observed at the graphene corners. Dirac 2 + 1 fermions with a linear scattering ratio (massless) can describe the Brillouin zone [19- 22]. This effect opens up the possibility of testing multiple aspects of relativistic phenomena that, in general, require a lot of energy in condensate physics experiments, such as chiral tunnels and the Klein paradox [24-25]. The aim of this study is to solve the 2D graphene as material in theoretical physics with the algebra of NC and we are going to treat it with the thermal properties of this system at high-temperature regime.

II. GRAPHENE IN NON-COMMUTATIVE GEOMETRY

Before proceeding to the solution of the graphene equation, we define some relations of the non-commutative space.

Non-commutative space is characterized by the fact that its coordinate operators are non-commutative, in contrast to the properties of the coordinates of ordinary space. The coordinates, in this case, satisfy the following relationships

$$[\hat{x}^{\mu}, \hat{y}^{v}] = i\theta^{\mu v} \tag{1}$$

Where $\theta^{\mu v}$is an antisymmetrical tensor in the usual quantum mechanics and plays an analogous function to $\hbar$.

We want to maintain the unity of the theory, we choose θ^{0v}=0 , which means that time remains as a parameter and that non-commutativity only affects physical space. The product of any two functions in the sense of this deformation is equivalent to the star Moyal product identified by

$$(f \star g)(x) = exp\left[\frac{i}{2}\theta_{ab}\partial x_a \partial y_b\right] f(x)g(y)\Big|_{x=y} \tag{2}$$

Where f and g are two arbitrary and considered to be infinitely distinct functions.

The effects of transition and momentum in this model can be expressed by the two transformations [26-28]:

$$x_i \longrightarrow x_i - \frac{1}{2\hbar}\theta_{ij}p_j \; and \; p_i \longrightarrow p_i, i = \overline{1,3} \tag{3}$$

With an antisymmetric tensorθ parameter, selected as

$$\theta_{ij} = \epsilon_{ijk}\theta_k \; and \; \theta_3 = \theta \tag{4}$$

We can rewrite the transformation based on this fact (3), in the following condensed form.

$$\theta_{12} = -\theta_{21} = \theta_3 = \theta \; with \; \vec{r} \rightarrow \vec{r} + \frac{\vec{\theta} \times \vec{p}}{2\hbar} \tag{5}$$

The electron in the quantum theory of graphene is a massless fermion that moves with a velocity $V_F = (1.12 \pm 0.02) \times 10^6 \, m\, s^{-1}$ called Fermi velocity verify the relativistic massless Dirac equation. The discovery of graphene gives us the opportunity of testing various effects of QED, such as the "Klein paradox" because this effect is unobservable in particle physics. In this section, we are interested in solving the (1 + 2)-dimensional massless

Dirac equation in the presence of an external constant magnetic field$A = \frac{B}{2}(-y, x, 0)$. In this case, the graphene equation read

$$(\hat{\boldsymbol{\alpha}}.\mathbf{p})\Psi(\mathrm{r}) = \frac{\boldsymbol{E}}{\boldsymbol{V_F}}\Psi(\mathrm{r}) \tag{6}$$

Where $\hat{\alpha}$ the usual Dirac matrice, given by

$$\hat{\boldsymbol{\alpha}} = \begin{pmatrix} \mathbf{0} & \hat{\boldsymbol{\sigma}} \\ \hat{\boldsymbol{\sigma}} & \mathbf{0} \end{pmatrix} \tag{7}$$

$\hat{\sigma}$ designates the Pauli matrices.

We may assume that the four-component spinor Ψ is of the form $\Psi(\mathrm{r}) = (\Psi_a(\mathrm{r}), \Psi_b(\mathrm{r}))$.

On substitution of Ψ (r) as given into (6), we get the following equations for the two-component spinors $\Psi_a(\mathrm{r})$ and $\Psi_b(\mathrm{r})$:

$$\begin{aligned} \hat{\boldsymbol{\sigma}}\boldsymbol{p}^{-}\boldsymbol{\Psi_b}(\mathbf{r}) &= \frac{\boldsymbol{E}}{\boldsymbol{V_F}}\boldsymbol{\Psi_a}(\mathbf{r}) \\ \hat{\boldsymbol{\sigma}}\boldsymbol{p}^{-}\boldsymbol{\Psi_a}(\mathbf{r}) &= \frac{\boldsymbol{E}}{\boldsymbol{V_F}}\boldsymbol{\Psi_b}(\mathbf{r}) \end{aligned} \tag{8}$$

With $p^{-} = p - eB \times \left(r + \frac{\theta \times p}{2\hbar}\right)$.

These two equations can be used to eliminate $\Psi_b(\mathrm{r})$in favor of$\Psi_a(\mathrm{r})$, so that we can have

$$(\hat{\boldsymbol{\sigma}}.\boldsymbol{p}^{-})(\hat{\boldsymbol{\sigma}}.\boldsymbol{p}^{-})\boldsymbol{\Psi_a}(\mathbf{r}) = \frac{\boldsymbol{E^2}}{\boldsymbol{V_F}^2}\boldsymbol{\Psi_a}(\mathbf{r}) \tag{9}$$

According to the following relations $(\hat{\sigma}.A)(\hat{\sigma}.B) = A.B + i\hat{\sigma}.(A \times B)$

The equation (9) can be written as

$$((\boldsymbol{p}^{-}.\boldsymbol{p}^{-}) + \boldsymbol{i\sigma}.(\boldsymbol{p}^{-} \times \boldsymbol{p}^{-}))\boldsymbol{\Psi_a}(\mathbf{r}) = \frac{\boldsymbol{E^2}}{\boldsymbol{V_F}^2}\boldsymbol{\Psi_a}(\mathbf{r}) \tag{10}$$

After a straightforward calculation of eq(10),we obtain

$$\begin{aligned} \left[\left(\mathbf{1} + \frac{\boldsymbol{eB\theta}}{\mathbf{2}\hbar} + \frac{\boldsymbol{e^2B^2\theta^2}}{\mathbf{16}\hbar^2}\right)\boldsymbol{p}^2 + \left(\frac{\boldsymbol{e^2B^2}}{\mathbf{4}}\right)\boldsymbol{r}^2 - \left(\boldsymbol{eB} + \frac{\boldsymbol{e^2B^2\theta^2}}{\mathbf{4}\hbar^2}\right)\boldsymbol{L_z}\right. \\ \left. - \left(\boldsymbol{eB}\hbar + \frac{\boldsymbol{e^2B^2\theta}}{\mathbf{4}}\right)\boldsymbol{\sigma_z} - \frac{\boldsymbol{E}^2}{\boldsymbol{V_F}^2}\right]\boldsymbol{\Psi_a}(\mathbf{r}) = \mathbf{0} \end{aligned} \tag{11}$$

To solve the eq.(11), we introduce the polar coordinates in position space (r, ϕ), and we use the following ansatz $\Psi_a(\mathrm{r}) = \exp(\mathrm{i}m_l\varphi)\mathrm{R}_{\mathrm{n,l}}(\mathrm{r})\chi_\tau$, where n is the radial quantum number, m_l, and $\tau = \pm 1$ are, respectively, the

eigenvalues of angular momentum and spin operators, and $\chi_{+1}^{T} = (1,0)$, $\chi_{-1}^{T} = (0,1)$ are the spin functions; to obtain

$$\left[\left(\frac{\mathbf{d}}{\mathbf{dr}}\right)^{2} + \frac{\mathbf{1}}{\boldsymbol{r}}\frac{\mathbf{d}}{\mathbf{dr}} - \frac{\mathbf{m_l^2}}{\mathbf{r}^2} - \frac{\boldsymbol{\eta}\mathbf{r}^2}{\hbar^2} + \boldsymbol{\varepsilon}\right]\mathbf{R_{n,l}(r)} = \mathbf{0} \tag{12}$$

While the parameters η, εare constants, we just name them after reorganizing the equation.

We use the appropriate transformations by employing a direct method in order to obtain the following energy spectrum such as:

$$\boldsymbol{E_{n,m_l}} = \frac{\hbar \boldsymbol{V_F}}{\boldsymbol{l_B}}\left[(\boldsymbol{2n} + \boldsymbol{m_l} + \mathbf{1})\sqrt{\left(\boldsymbol{l_B}^4 + \frac{\boldsymbol{\theta}\boldsymbol{l_B}^2}{\mathbf{2}} + \frac{\boldsymbol{\theta}^2}{\mathbf{16}}\right)} - \boldsymbol{\tau}\left(\mathbf{1} + \frac{\boldsymbol{\theta}^2}{\mathbf{4}\boldsymbol{l_B}}\right) - \boldsymbol{m_l}\left(\boldsymbol{l_B} + \frac{\boldsymbol{\theta}^2}{\mathbf{4}\hbar\boldsymbol{l_B}}\right)\right]^{\mathbf{1/2}} \tag{13}$$

In addition, we notice here that $l_B = \sqrt{\hbar/eB}$ is called magnetic length.

Moving to the wave function, which gives such

$$\boldsymbol{\psi_a(r,\phi)} = \boldsymbol{Cr^{-\frac{1}{2}}exp}\left(-\frac{\boldsymbol{r^2}}{\boldsymbol{a^2}}\right)(-\boldsymbol{n},\frac{\mathbf{3}}{\mathbf{4}} + \frac{\boldsymbol{m_l}}{\mathbf{2}},\frac{\boldsymbol{r^2}}{\boldsymbol{a^2}})\frac{\boldsymbol{r}^{\mathbf{2}\frac{\mathbf{1}}{\mathbf{4}}+\frac{\boldsymbol{m_l}}{\mathbf{2}}}}{\boldsymbol{a^2}}\boldsymbol{F}(-\boldsymbol{n},\frac{\mathbf{3}}{\mathbf{4}} + \frac{\boldsymbol{m_l}}{\mathbf{2}},\frac{\boldsymbol{r^2}}{\boldsymbol{a^2}})\boldsymbol{exp(il\phi)} \tag{14}$$

If we test these obtained results by putting$\theta = 0$, we get the ordinary case in the commutative space.

III. THERMODYNAMIC PROPERTIES

In this section, we examine the effect of non-commutative geometry on the thermal properties of Graphene . Returning to the spectrum (13) which can be written as:

$$E_n = \pm mc^2\sqrt{\mu n + \lambda} \tag{15}$$

Because all the thermodynamic quantities can be obtained from the Z partition function, we first calculate this function of the system, which is defined according to the temperature T as

$$Z(V,T) = \sum_{n=0}^{\infty} e^{-\beta(E_n - E_0)} \tag{16}$$

With$\beta = \frac{1}{k_B T}$, k_B is the Boltzmann constant, and E_0 is ground state energy. *(l=0)*

In addition, for the states of negative energy, the function of the Z-partition of the oscillator of Graphene at finite temperature T has the form:

$$Z(V,T) = \sum_{n=0}^{\infty} e^{\beta mc^2(\sqrt{\mu n+\lambda}-\sqrt{\lambda})} = e^{-\beta mc^2\sqrt{\lambda}} \sum_{n=0}^{\infty} e^{\beta mc^2(\sqrt{\mu n+\lambda})} \quad (17)$$

Now, to evaluate this function, we use the formula Euler-Maclaurin. For carrying out our analysis on the thermodynamics of the massless Dirac, we will limit to the stationary states of positive energy

By replacing (15) in (17), we obtain the partition function of graphene in deformed space as:

$$Z(V,T) = \sum_{n=0}^{\infty} e^{-\beta mc^2(\sqrt{\mu n+\lambda}-\sqrt{\lambda})} = e^{\beta mc^2\sqrt{\lambda}} \sum_{n=0}^{\infty} e^{-\beta mc^2(\sqrt{\mu n+\lambda})} \quad (18)$$

Then we employ Euler-Maclaurin formula; we obtain the partition function:

$$Z = \frac{1}{2} + \frac{2\sqrt{\lambda}}{\mu}\tau + \frac{2}{\mu}\tau^2 + \left(\frac{\mu}{24\sqrt{\lambda}} - \frac{\mu^3}{1920\sqrt{\lambda^5}}\right)\frac{1}{\tau} - \frac{\mu^3}{1920\lambda^2}\frac{1}{\tau^2} - \frac{\mu^3}{5760\sqrt{\lambda^3}}\frac{1}{\tau^3} \quad (19)$$

Where $\tau = \frac{1}{\beta mc^2} = \frac{k_B T}{mc^2}$

The thermodynamic properties of the physical system, such as free energy F, mean energy U specific heat C, and entropy S, can be calculated from the following expressions:

$$F = -\frac{1}{\beta} lnZ \, , U = K_B T^2 \frac{\partial lnZ}{\partial T} \quad , C = \frac{\partial U}{\partial T} \, , and$$

$$S = -\frac{\partial F}{\partial T}. \quad (20)$$

Such:

$$F = -mc^2 \tau lnZ \quad (21)$$

Following the same manner to obtain the other properties. In the following, all the profiles of the thermodynamic quantities as a function of the temperature variable were presented for different values of the deformation parameter θ

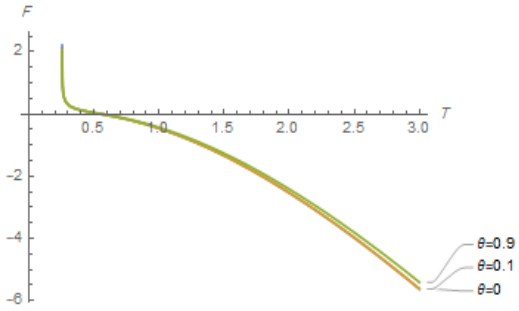

Figure 1: The free energy F as a function of T for deformation values.θ

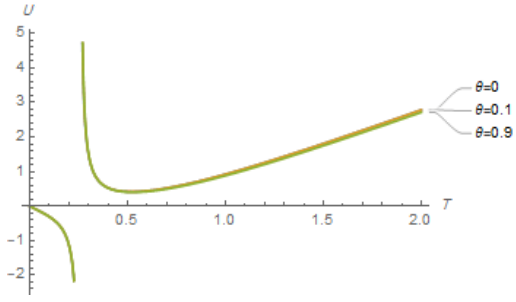

Figure 2: The mean energy U as a function of T for deformation values.θ

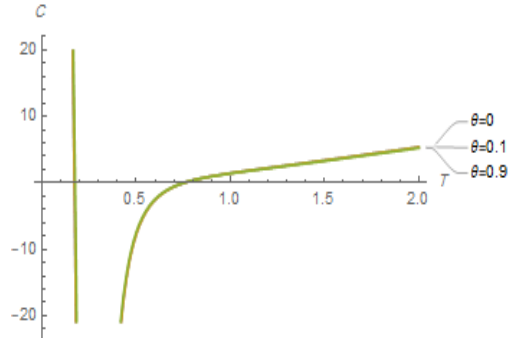

Figure 3: The heat capacity C as a function of T for deformation values.θ

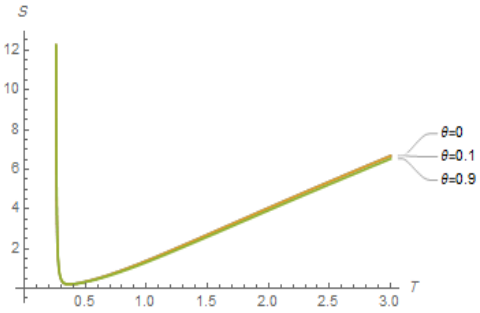

Figure 4: The entropy S as a function of T for deformation values.θ

Where we have used the Hartree atomic units ($\hbar = c = K_B = \omega = B = m = 1$)
We observe that the thermodynamic properties have influenced by the parameter θ.

IV. CONCLUSION

We investigated the exact solution of the 2D massless Dirac equation in the presence of an external magnetic field in the commutation relations of noncommutative geometry in this work, where we obtained the energy eigenvalues and the wave function of the system using a direct method. Finally, we concluded that the system was influenced by NC geometry and produced the results found in the literature when =0.Also, we have studied the thermodynamic properties of the system in the high temperature regime using the partition function Z and we concluded that the system has been influenced by the NC algebra.

REFERENCES

[1]. Mokhtar Falek.M Merad,DKP Oscillator in a Noncommutative Space ,October 2008.Communications in Theoretical Physics 50(3):587.
[2]. H. S. Snyder, Quantized space-time, Phys. Rev. 71, 38–41 (1947)
[3]. T. Banks, W. Fischler, S. H. Shenker and L. Susskind, M theory as a matrix model: a conjecture, Phys. Rev. D 55, 5112–5128 (1997)
[4]. N. Seiberg and E. Witten, String theory and noncommutative geometry, JHEP 1999, 32 (1999)
[5]. F. Lizzi, G. Mangano, G. Miele, and M. Peloso, Cosmological perturbations and short distance physics from noncommutative geometry, JHEP 2002, 49 (2002)
[6]. R. Brandenberger and P.-M. Ho, Noncommutative spacetime, stringy spacetime uncertainty principle, and density fluctuations, Phys. Rev. D 66, 023517 (2002)
[7]. B. Vakili, N. Khosravi and H. R. Sepangi, Bianchi spacetimes in noncommutative phase space, Class. Quant. Grav. 24, 931–949 (2007)

[8]. S. Minwalla, M. van Raamsdonk and N. Seiberg, Noncommutative perturbative dynamics, JHEP 2000, 20 (2000)
[9]. S. M. Carroll, J. A. Harvey, V. A. Kostelecky, C. D. Lane and T. Okamoto, Noncommutative field theory and Lorentz violation, Phys. Rev. Lett. 87, 141601 (2001)
[10]. R. J. Szabo, Quantum field theory on noncommutative spaces, Phys. Rep. 378, 207–299 (2003)
[11]. M. R. Douglas and N. A. Nekrasov, Noncommutative field theory, Rev. Mod. Phys. 73, 977–1029 (2001)
[12]. J. Gamboa, M. Loewe and J. C. Rojas, Noncommutative quantum mechanics, Phys. Rev. D 64, 067901 (2001)
[13]. M. Przanowski and J. Tosiek, The Weyl-Wigner-Moyal formalism. III. The generalized Moyal product in the curved phase space," Acta Phys. Pol. B 30, 179 (1999)
[14]. B. Mirza and M. Mohadesi, The Klein-Gordon and the Dirac oscillators in a noncommutative space, Comm. Theor. Phys. 42, 664–668 (2004)
[15]. D. J. Gross and P. F. Mende, String theory beyond the Planck scale, Nucl. Phys. B 303, 407–454 (1988)
[16]. D. Amati, M. Ciafaloni and G. Veneziano, Can spacetime be probed below the string size? Phys. Lett. B 216, 41–47 (1989)
[17]. M. Maggiore, The algebraic structure of the generalized uncertainty principle, Phys. Lett. B 319, 83–86 (1993)
[18]. G. Amelino-Camelia, N. E. Mavromatos, J. Ellis and D. V. Nanopoulos, On the space-time uncertainty relations of Liouville strings and D-branes, Mod. Phys. Lett. A 12, 2029–2035 (1997)
[19]. Novoselov, K. S., Geim, A. K., Morozov, S. V., Jiang, D. E., Zhang, Y., Dubonos, S. V. & Firsov, A. A. (2004). Electric field effect in atomically thin carbon films. *science*, *306*(5696), 666-669
[20]. K.S. Novoselov, et al., Proc. Natl. Acad. Sci. 102 (2005) 10451.
[21] A.H. Castro Neto, F. Guinea, N.M.R. Peres, K.S. Novoselov, A.K. Geim, Rev. Modern Phys. 81 (2009) 109.
[22] N. Peres, Rev. Modern Phys. 82 (2010) 2673.
[23] Charles L. Fefferman, Michael I. Weinstein, J. Amer. Math. Soc. 25 (2012) 1169.
[24] M.I. Katsnelson, K.S. Novoselov, A.K. Geim, Nat. Phys. 2 (2006) 620.
[25] M.I. Katsnelson, Mater. Today 10 (2007) 20
[26]S. Jing, F. Zuo and T. Heng, Deformation quantization of noncommutative quantum mechanics, JHEP 0410 (2004) 049.
[27]J. Gamboa, M. Loewe, F. Mendez and J.C. Rojas, Noncommutative Quantum Mechanics: The Two-Dimensional Central Field,Int. J. Mod. Phys. A 17, 2555 (2002)
[28]J. Gamboa, M. Loewe, F. Mendez and J.C. Rojas,The Landau problem and noncommutative quantum mechanics, Mod. Phys. Lett. A 16, 2075 (2001)